Research Article | Vol. 25, No. 5 | 6 Mar 2017 | OPTICS EXPRESS 5440

Optics EXPRESS

Monolithic optical link in silicon-on-insulator CMOS technology

SATADAL DUTTA,[1,*] VISHAL AGARWAL,[2] RAYMOND J.E. HUETING,[1] JURRIAAN SCHMITZ,[1] AND ANNE-JOHAN ANNEMA[2]

[1]*Semiconductor Components, MESA+ Institute for Nanotechnology, University of Twente, 7500 AE, Enschede, The Netherlands*

[2]*Integrated Circuit Design, CTIT, University of Twente, 7500 AE, Enschede, The Netherlands*

[*]*s.dutta@utwente.nl*

Abstract: This work presents a monolithic laterally-coupled wide-spectrum (350 nm $< \lambda <$ 1270 nm) optical link in a silicon-on-insulator CMOS technology. The link consists of a silicon (Si) light-emitting diode (LED) as the optical source and a Si photodiode (PD) as the detector; both realized by vertical abrupt n^+p junctions, separated by a shallow trench isolation composed of silicon dioxide. Medium trench isolation around the devices along with the buried oxide layer provides galvanic isolation. Optical coupling in both avalanche-mode and forward-mode operation of the LED are analyzed for various designs and bias conditions. From both DC and pulsed transient measurements, it is further shown that heating in the avalanche-mode LED leads to a slow thermal coupling to the PD with time constants in the ms range. An integrated heat sink in the same technology leads to a ~ 6 times reduction in the change in PD junction temperature per unit electrical power dissipated in the avalanche-mode LED. The analysis paves way for wide-spectrum optical links integrated in smart power technologies.

OCIS codes: (040.6040) Silicon; (130.0250) Optoelectronics; (230.3670) Light-emitting diodes; (230.5170) Photodiodes; (130.0130) Integrated optics; (040.1880) Detection; (120.6810) Thermal effects.

References and links

1. X. Zheng, D. Patil, J. Lexau, F. Liu, G. Li, H. Thacker, Y. Luo, I. Shubin,J. Li, J. Yao, P. Dong, D. Feng, M. Asghari, T. Pinguet, A. Mekis, P. Amberg, M. Dayringer, J. Gainsley, H.F. Moghadam, E. Alon, K. Raj, R. Ho, J. E. Cunningham, and A. V. Krishnamoorthy, "Ultra-efficient 10 Gb/s hybrid integrated silicon photonic transmitter and receiver," Opt. Express, **19**(6), 5172–5186 (2011).
2. N. Rouger, L. T. Le, D. Colin and J.-C. Crébier, "CMOS SOI Gate Driver with Integrated Optical Supply and Optical Driving for Fast Power Transistors," in *Proc. 28th International Symposium on Power Semiconductor Devices* (2016), pp. 427–430.
3. N. Van-Sang, L. Thang-Long, F. Sarrafin, T. Ngoc-Duc, D. Colin, N. Rouger, P. LeFranc, Y. Lembeye, J-D. Arnould, B. Allard and J-C. Crebier, "Contributions to dedicated gate driver circuitry for very high switching speed high temperature power devices," in *Proc. 28th International Symposium on Power Semiconductor Devices* (2016), pp. 443–446.
4. M.A. Green, J. Zhao, A. Wang, P.J. Reece and M. Gal, "Efficient silicon light-emitting diodes," Nature **412**, 805–808 (2001).
5. T. Hoang, P. LeMinh, J. Holleman, V. Zieren, M.J. Goossens and J. Schmitz, "A high efficiency lateral light emitting device on SOI," in *Proc. 12th IEEE International Symposium on Electron Devices for Microwave and Optoelectronic Applications* (2004), pp. 87–91.
6. C. Schinke, D. Hinken, J. Schmidt, K. Bothe and R. Brendel, "Modeling the spectral luminescence emission of silicon solar cells and wafers," IEEE J. Photovoltaics **3**(3), 1038–1052 (2013).
7. G. Piccolo, P. I. Kuindersma, L.-A. Ragnarsson, R. J. E. Hueting, N. Collaert, and J. Schmitz, "Silicon LEDs in FinFET technology," in *Proc. 44th ESSDERC* (2014), pp. 274–277.
8. B.P. van Drieënhuizen and R.F. Wolffenbuttel, "Optocoupler based on the avalanche light emission in silicon," Sensors Actuators A **31**, 229–240 (1992).
9. J. Schmitz, R. de Vries, C. Salm, T. Hoang, R. Hueting, and J. Holleman, "On the switching speed of SOI LEDs," in Proc. EUROSOI (2008), pp. 101–102.
10. A. G. Chynoweth and K. G. McKay, "Photon emission from Avalanche Breakdown in Silicon," Phys. Rev. **102**(2), 369–376 (1956).

#281670 https://doi.org/10.1364/OE.25.005440
Journal © 2017 Received 28 Nov 2016; revised 21 Jan 2017; accepted 18 Feb 2017; published 28 Feb 2017

Optics EXPRESS

11. M. du Plessis, H. Aharoni, and L. W. Snyman, "Silicon LEDs fabricated in standard VLSI technology as components for all silicon monolithic integrated optoelectronic systems," IEEE J. Sel. Topics Quantum Electron. **8**(6), 1412–1419 (2002).
12. L.W. Snyman, M. du Plessis, and H. Aharoni, "Injection-Avalanche-Based n^+pn Silicon Complementary Metal Oxide Semiconductor Light-Emitting Device (450 - 750 nm) with 2-Order-of-Magnitude Increase in Light Emission Intensity," Jpn. J. Appl. Phys. **46**(4B), 2474–2480 (2007).
13. S. Dutta, R. J. E. Hueting, A. J. Annema, L. Qi, L. K. Nanver, and J. Schmitz, "Opto-electronic modeling of light emission from avalanche-mode silicon p^+n junctions," J. Appl. Phys. **118**, 114506 (2015).
14. A. Chatterjee, B. Bhuva, and R. Schrimpf, "High-speed light Modulation in avalanche breakdown mode for Si diodes," IEEE Electron Dev. Lett. **25**(9), 628–630 (2004).
15. H-C. Lee and C-K. Liu, "Si-based current-density-enhanced light emission and low-operating-voltage light-emitting/receiving designs," Solid State Electron. **49**, 1172–1178 (2005).
16. M. Sergio and E. Charbon, "An intra-chip electro-optical channel based on CMOS single photon detectors," in *IEEE International Electron Devices Meeting Tech. Digest* (2005), pp. 822.
17. B. Huang, X. Zhang, W. Wang, Z. Dong, N. Guan, Z. Zhang, and H. Chen, "CMOS monolithic optoelectronic integrated circuit for on-chip optical interconnection," Opt. Commun. **284**, 3924–3927 (2011).
18. A. Khanmohammadi, R. Enne, M. Hofbauer, and H. Zimmermann, "Monolithic integrated optical random pulse generator in high voltage CMOS technology," in *Proc. ESSDERC 2015* (2015), pp. 138–141.
19. L.W. Snyman, H. Aharoni, A. Biber, A. Bogalecki, L. Canning, M. du Plessis and P. Maree, "Optical sources, integrated optical detectors, and optical waveguides in standard silicon CMOS integrated circuitry," Proc. SPIE **3953**, 20–36 (2000).
20. K. Xu, B. Huang, K.A. Ogudo, L.W. Snyman, H. Chen, and G.P. Li, "Silicon Light-emitting Device in Standard CMOS technology," in *Proc. 8th International Photonics and OptoElectronics Meetings* (2015).
21. D. Li, W. Li, L. Duan, G. Zhang, S. Liu, and G. Dong, "Highly integrable organic optocouplers on a patterned double-side indium tin oxide substrate with high isolation voltage," IEEE Electron Device Lett. **36**(2), 171–173 (2015).
22. R. Dangel, J. Hofrichter, F. Horst, D. Jubin, A. La Porta, N. Meier, I. M. Soganci, J. Weiss, and B. J. Offrein, "Polymer waveguides for electro-optical integration in data centers and high-performance computers," Opt. Express **23**(4), 4736–4750 (2015).
23. J. Chen, N. Bamiedakis, P. Vasil'ev, T. Edwards, C. Brown, R. Penty, and I. White, "High-bandwidth and large coupling tolerance graded-index multimode polymer waveguides for on-board high-speed optical interconnects," J. Lightwave Technol. **34**(12), 2934–2940 (2015).
24. P. Wessels, M. Swanenberg, H. van Zwol, B. Krabbenborg, H. Boezen, M. Berkhout, and A. Grakist, "Advanced BCD technology for automotive, audio and power applications," Solid-State Electronics **51**, 195–211 (2007).
25. S. Mandai, M. W. Fishburn, Y. Maruyama, and E. Charbon, "A wide spectral range single-photon avalanche diode fabricated in an advanced 180 nm CMOS technology," Opt. Express **20**(6), 5849–5857 (2012).
26. M-J. Lee, P. Sun, and E. Charbon, "A first single-photon avalanche diode fabricated in standard SOI CMOS technology with a full characterization of the device," Opt. Express **23**(10), 13200–13209 (2015).
27. S. Dutta, R.J.E. Hueting, V. Agarwal and A.J. Annema, "An integrated optical link in 140 nm SOI technology," in *Proc. Conference on Lasers and Electro-Optics, Session JW2A* (2016), paper 132.
28. B. G. Streetman and S. K. Banerjee, *Solid State Electronic Devices,* 6th ed. (PHI Learning Pvt. Ltd., 2009).
29. David J. Griffiths, *Introduction to Electrodynamics,* 3rd. ed. (Pearson Education, 1999).
30. L. Yan, G. Koops, P. Steeneken, A. Heringa, R. Surdeanu, and L. van Dijk, "Integrated heat sinks for SOI power devices," in *Proc. 25th ISPSD* (2013), pp. 285–288.
31. R. F. Pierret, *Semiconductor Device Fundamentals* (Addison-Wesley Publ., 1996).
32. M. Lahbabi, A. Ahaitouf, M. Fliyou, E. Abarkan, J.-P. Charles, A. Bath, A. Hoffmann, S. E. Kerns, and D. V. Kerns, Jr., "Analysis of electroluminescence spectra of silicon and gallium arsenide p-n junctions in avalanche breakdown," J. Appl. Phys. **95**(4), 1822–1828 (2004).
33. M. A. Green, "Self-consistent optical parameters of intrinsic silicon at 300 K including temperature coefficients," Solar Energy Mater. Solar Cells **92**, 1305–1310 (2008).
34. G.E. Giakoumakis, "Matching factors for various light-source-photodetector combinations," Appl. Phys. A **52**, 7–9 (1991).
35. E. F. Schubert, *Light Emitting Diodes* (Cambridge University Press, 2006).
36. K. Rajkanan, R. Singh, and J. Schewchun, "Absorption coefficient of silicon for solar cell calculations," Solid-State Electronics **22**, 793–795 (1979).
37. V. Puliyankot and R.J.E. Hueting, "One-dimensional physical model to predict the internal quantum efficiency of Si-based LEDs," IEEE Trans. Electron. Devices **59**(1), 26–34 (2012).
38. K. A. Ogudo, D. Schmieder, D. Foty, and L. W. Snyman, "Optical propagation and refraction in silicon complementary metal-oxide-semiconductor structures at 750 nm: toward on-chip optical links and microphotonic systems," J. Micro/Nanolith. MEMS MOEMS **12**(1), 013015 (2013).
39. I.H. Malitson, "Interspecimen comparison of the refractive index of fused silica," J. Opt. Soc. Am. **55**, 1205–1208 (1965).
40. M.J. Adams, "Loss calculations in weakly-guiding optical dielectric waveguides," Opt. Commun. **23**(1), 105–108

Optics EXPRESS

(1977).
41. R.J.E. Hueting, A. Heringa, B.K. Boksteen, S. Dutta, A. Ferrara, V. Agarwal, and A.J. Annema, "An improved analytical model for carrier multiplication near breakdown in diodes," IEEE Trans. Electron Devices **64**(1), 264–270 (2017).
42. L.T. Su, J.E. Chung, D.A. Antoniadis, K.E. Goodson and M.I. Flik, "Measurement and modeling of self-heating in SOI nMOSFET's," IEEE Trans. Electron Devices **41**(1), 69–75 (1994).
43. W. Jin, W. Liu, S.K.H. Fung, P.C.H. Chan and C. Hu, "SOI thermal impedance extraction methodology and its significance for circuit simulation," IEEE Trans. Electron Devices **48**(4), 730–736 (2001).
44. M.B. Kleiner, S.A. Kühn and W. Weber, "Thermal conductivity of thin silicon dioxide films in integrated circuits," in *Proc. ESSDERC* (1995), pp. 473–476.
45. M. Asheghi, K. Kurabayashi, R. Kasnavi and K.E. Goodson, "Thermal conduction in doped single-crystal silicon films," J. Appl. Phys. **91**, 5079–5088 (2002).
46. S. Radovanovic, A.J. Annema, and B. Nauta, "A 3 Gb/s optical detector in standard CMOS for 850 nm optical communication," IEEE J. Solid-State Circuits **40**(8), 1706–1717 (2005).

1. Introduction

Monolithically integrated optical interconnects cater to high speed transceiver [1] applications, and to smart-power applications where data needs to be transferred between galvanically isolated voltage domains [2, 3]. The viability of an integrated optical link in silicon (Si) demands a high coupling efficiency (that encompasses the combined efficiencies of the light-emitter, waveguide and the detector) in conjunction with proper galvanic isolation and sufficiently high data rates. Operating a Si light-emitting diode (LED) in forward mode (FM) yields infrared (IR) electroluminescence (EL) ($\lambda \sim$ 1000-1270 nm) [4–7]. This emission spectrum has a small overlap with the spectral responsivity of Si photodiodes (PDs) [8] resulting in a low internal quantum efficiency (IQE) of the PD. Modulation speeds up to $\sim$ 1 MHz have been reported for Si FMLEDs [9].

Operating a Si LED in avalanche mode (AM) yields broad-spectrum EL ($\lambda \sim$ 350-900 nm) [10–13] with a reported IQE of $\sim 10^{-5}$ [12]. This EL spectrum has a significant overlap with the spectral responsivity of Si (PDs) [8] resulting in a high IQE of the PD. Optical modulation speeds as high as a few tens of GHz have been reported in Si AMLEDs [14].

Galvanic isolation can be obtained using silicon-on-insulator (SOI) technology. Prior art reported FM optocoupling [15] and AM optocoupling in a 0.8 μm [16], 0.35 μm [17, 18], 2 μm [19] and 3 μm [20] bulk CMOS technology with limited galvanic isolation. High isolation voltages ($\sim$ 3 kV) have been reported [21], however in an organic optocoupler which is not compatible with standard CMOS technology. Here, a maximum on-off keying speed of only 70 kHz was reached. SOI technology also offers monolithic waveguiding, which has shown potential applications in high-level hybrid integration for cost-effective high-performance computing [22, 23]. Significant advances have been made to integrate optical data communication in the past, but most of them utilized hybrid solutions for inter-chip data transfer [1, 23]. In this work:

1. A fully integrated wide-spectrum (350 nm $< \lambda <$ 1270 nm) optical link in a commercial 0.14 μm SOI-CMOS technology [24] is demonstrated, which provides $\sim$ 100 V galvanic isolation. The link has three components: The light-emitter, the optical channel (waveguide) and the detector. The LED and the PD are implemented as vertical n^+p junctions in Si.

2. Optocoupling is shown with the LED biased both in FM and in AM, the two yielding considerably different link properties with respect to link efficiencies in DC operation, parasitic thermal coupling effects and scaling properties.

3. We aim at integrated optical interconnects for smart power applications (e.g. level shifters) which requires highly sensitive photodetectors (e.g. SPADs [25, 26]) given the inherently low light intensity emitted by the LEDs. However, to demonstrate and benchmark our design, we use regular PDs.

Optics EXPRESS

This paper is an extension of a recent conference contribution [27] and is outlined as follows. Section 2 presents the design and layout of our optical link. Here the main parameters that contribute to the overall link efficiency are defined. Section 3 describes the DC electrical and EL properties of the LED. Section 4 describes the spectral responsivity of the PD and its *I-V* characteristics. Sections 5 and 6 demonstrate optical coupling in DC operation of FM and AM operation of the LED. Section 7 addresses the heating in the AMLED, and thermal coupling to the PD. Section 8 presents a comparison between FM and AM operation of our optical link, followed by design recommendations for further improvement of the coupling quantum efficiency. Finally, section 9 concludes our work.

2. Architecture and layout

Figure 1(a) shows the schematic top-view of the optical link consisting of the LED, the dielectric channel (as a waveguide) and the PD. We use the ratio of the LED current I_{LED} to the short-circuit current (I_{SC}) of the PD [28] (the latter defined as photo-generated current at zero bias voltage) as a measure for the lateral optical coupling. We introduce the coupling quantum efficiency η as a figure-of-merit (FOM) of our designs, defined as:

$$\eta = \frac{I_{\mathrm{SC}}}{I_{\mathrm{LED}}} = \eta_{\mathrm{LED}} \cdot \eta_{\mathrm{WG}}(D) \cdot \eta_{\mathrm{PD}}, \tag{1}$$

where η_{LED} and η_{PD} represent the IQE of the LED and the PD respectively. $\eta_{\mathrm{WG}}(D)$ is a lumped representation of the overall efficiency of the waveguide (WG) which depends on the mode of LED operation, and on the link length D. $\eta_{\mathrm{WG}}(D)$ can be expressed as the product of various components: $\eta_{\mathrm{WG}}(D) = \eta_{\mathrm{in}} \cdot T_{\mathrm{Fresnel}} \cdot \eta_{\mathrm{prop}}(D) \cdot \eta_{\mathrm{out}}$. Here, η_{in} and η_{out} are the efficiencies of extraction of light from the LED to the WG, and that of capture of light from the WG to the PD respectively. T_{Fresnel} represents the effective transmission efficiency due to Fresnel reflections [29] at the Si-WG interfaces. Values of η_{in}, η_{out} and T_{Fresnel} are constants (independent of D) specific to our design and to the mode of LED operation, the detailed calculations of which will not be addressed in this paper. $\eta_{\mathrm{prop}}(D)$ is the D-dependent propagation efficiency and takes into account the absorptive losses in the WG and the effective angular aperture of the PD along the direction of propagation. η_{prop} will be further discussed in sections 5 and 6.

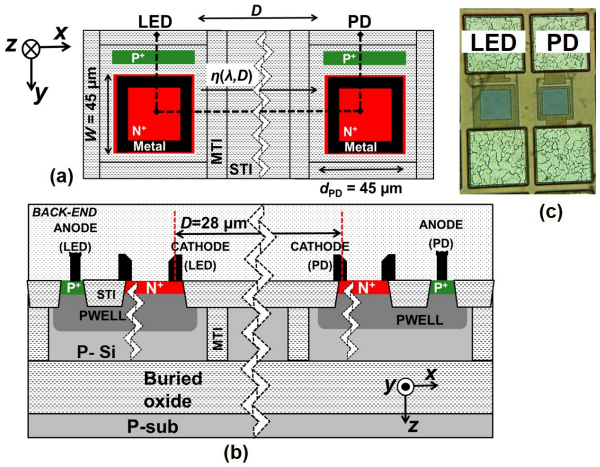

Fig. 1. (a) Schematic layout of our optical link. (b) Schematic vertical cross section of the default design of the link along the indicated dashed line in the layout. (c) Die micrograph (top-view) of the default design of our optical link. Figures (a) and (b) are not to scale.

Optics EXPRESS

Our optical link involves relatively low values of η, thereby demanding high electrical power, in particular during AM operation of the LED. This leads to a significant electrical power dissipation, and thereby heating in the AMLED.

Figure 1(b) shows the schematic vertical cross section of the default design of our optical link along the dashed line in Fig. 1(b). Figure 1(c) shows the die-micrograph. The LED and the PD consist of vertical abrupt n^+p junctions enclosed by medium trench isolation (MTI) for galvanic isolation down to the buried oxide layer. The substrate is lowly p-doped Si. A vertical window is opened in the cathode (n^+) contact and silicide layer formation is suppressed in the active areas (except at the contacts) to enable vertical measurement of the EL-spectra through an optical fiber. The LED and PD are separated using STI (composed of SiO_2). In addition, a variation of the link has been designed by placing a heat sink to its vicinity. This heat sink is a handle wafer contact [30], which is a vertical polysilicon column extending from the active SOI layer down to the handle wafer. In this design, D is varied from 10 μm to 60 μm in steps of 10 μm.

3. LED: electrical and optical behavior

The optical link is operated with the Si LED either in FM or AM. Figure 2 shows the I-V characteristics of the LED on a semi-log scale, measured at an ambient temperature T_0=300 K. An almost unity ideality factor is obtained for forward bias voltages < 0.8 V, while the series resistance becomes prominent for at a higher bias. In reverse bias, the current rises sharply near the avalanche breakdown voltage (V_{BR}). Using the definition of breakdown at an arbitrarily chosen current [31] I=1 μA, we find V_{BR} = 16.8 V.

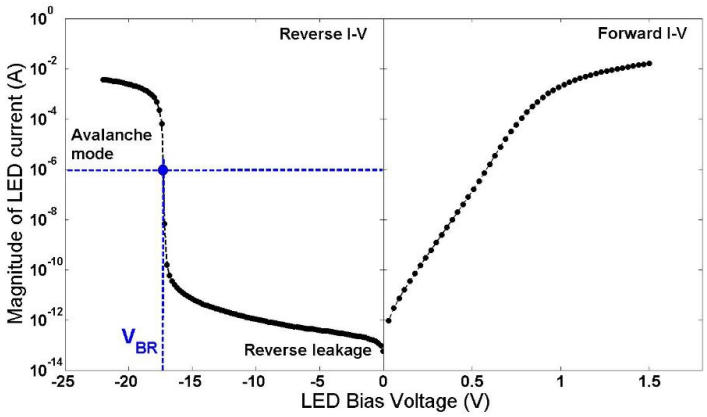

Fig. 2. Measured I-V characteristics of the LED at T_0=300 K in reverse and forward bias on a semi-log scale. Measurements are done using a Keithley 4200 SCS.

The EL micrographs in AM and FM LED operation are depicted in Figs. 3 (a) and 3(b), respectively. In particular for the AMLED, the emission dominates along the n^+ edge closest to the p^+ contact due to current crowding and field enhancement. In Fig. 3(b), we see the IR light emission extending well outside the diode's junction area, in line with the longer absorption length for IR light in Si. Figures 3(c) and 3(d) show the EL-spectra of the AMLED and the FMLED respectively at various current levels at T_0=300 K. The FMLED emits in the IR (~1000-1270 nm) [4–7]. The AMLED exhibits broad-spectrum (~350-900 nm) EL, similar to the ones reported and modeled earlier [13, 32]. Ripples are observed in the AM EL-spectra in the range 600 nm < λ < 800 nm, which appear due to Fabry-Perot interference in the back-end. The optical intensity increases linearly with increasing I_{FMLED} or I_{AMLED}.

Optics EXPRESS

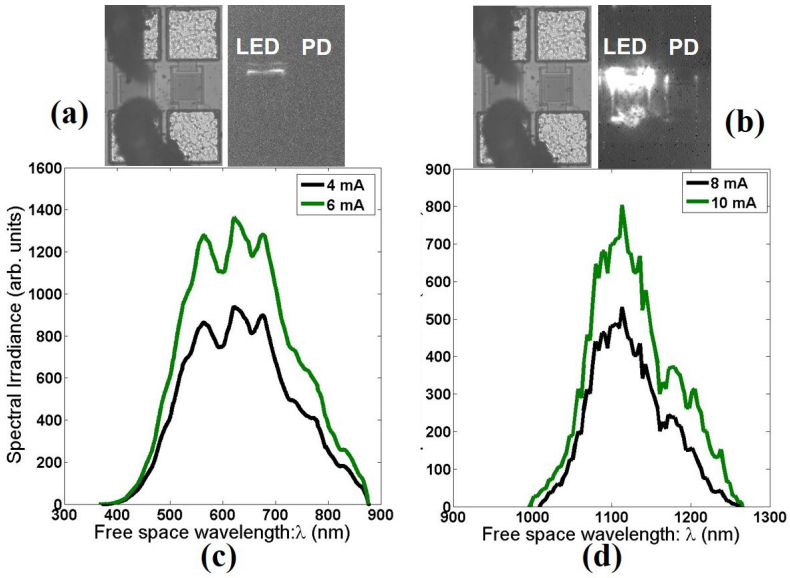

Fig. 3. Magnified die top-view along with the corresponding EL-micrographs for (a) the AMLED captured with a XEVA-257 camera and (b) for the FMLED captured vertically with a XEVA-320 InGaAs camera from Xenics. (c) EL-spectra of the LED at various current levels at T_0= 300 K for avalanche mode and (d) forward mode operation, measured vertically by a 50 μm multi-mode optical fiber feeding an ADC-1000-USB spectrometer (for AM-EL) and an AvaSpec-NIR256-1.7 spectrometer (for FM-EL) from Avantes. The arbitrary units in (c) and (d) are independent.

4. PD: electrical and optical behavior

The PD current (I_{PD}) is sensitive to both EL-intensity L (dependent on λ) and the junction temperature T_j [28]. It is the sum of the regular junction current and the photo-generated current (equal to I_{SC}):

$$I_{PD} = I_0(T_j) \cdot \left[\exp\left(\frac{qV_{PD}}{k_B T_j}\right) - 1\right] - I_{SC}(L, \alpha_{Si}(\lambda, T_j)), \tag{2}$$

where $I_{SC}(L, \alpha_{Si}(\lambda, T_j)) = -I_{PD}$ at $V_{PD} = 0$, with the negative sign representing current flow from the cathode to the anode. I_{SC} depends on L and on the Si absorption coefficient $\alpha_{Si}(\lambda, T_j)$. Also, q is the elementary charge and k_B is the Boltzmann constant, and I_0 is the dark current of the PD. Upon rearranging Eq. (2), the open-circuit voltage V_{OC} can be expressed in terms of I_{SC}:

$$V_{OC}(L, T_j) = \left(\frac{k_B T_j}{q}\right) \cdot \ln\left[1 + \frac{I_{SC}(L, \alpha_{Si}(\lambda, T_j))}{I_0(T_j)}\right]. \tag{3}$$

An increase in only L at a fixed T_j leads to an increase in both I_{SC} and V_{OC}. An increase in only T_j at a fixed L also results in an increase in the I_{SC} since $\alpha_{Si}(\lambda, T_j)$ increases with temperature [33], but V_{OC} decreases with increasing T_j. In AM operation of the LED, the higher electrical power leads to heating in the AMLED. This in turn leads to a rise T_j (not observed in FM operation). This is reflected from the I-V characteristics of the PD for various I_{AMLED} in our default design (without heat sink) as shown in Fig. 4.

Optics EXPRESS

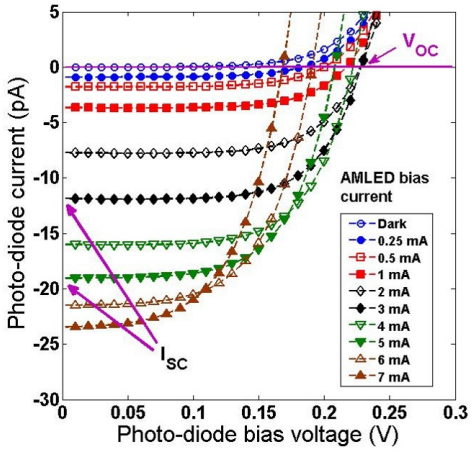

Fig. 4. *I-V* characteristics of the PD under AMLED operation at T_0=300 K for various I_{AMLED} for the default design without heat sink. I_{SC} increases with increasing I_{AMLED}. V_{OC} first increases and then decreases for higher I_{AMLED}, an indication of junction heating. Measurements are done using a Keithley 4200 SCS.

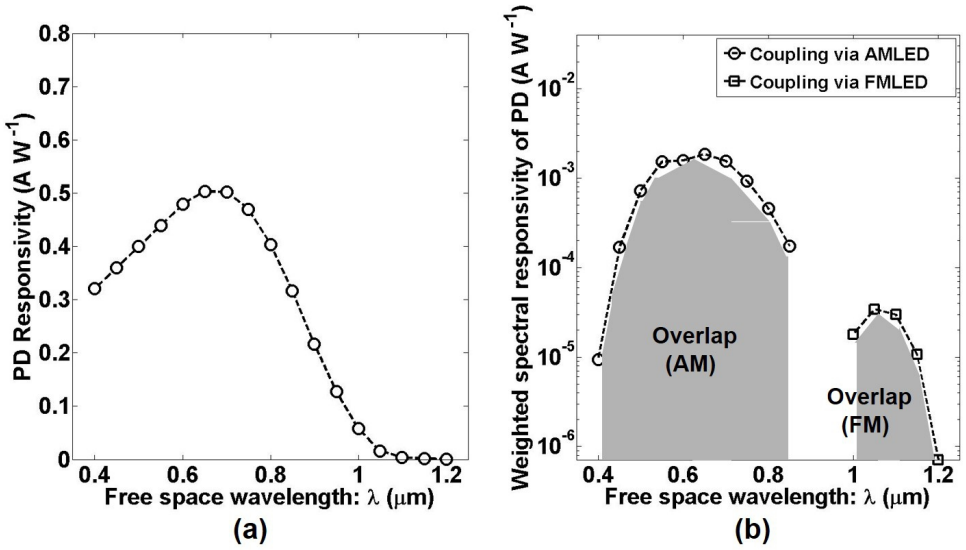

Fig. 5. (a) TCAD simulated PD responsivity at T_0 = 300 K as a function of photon wavelength when the junction is illuminated by a monochromatic, unpolarized and unidirectional light source at a fixed optical power P_{opt}. (b) Calculated responsivity of the PD weighted by the normalized spectral irradiance of the LED in AM and FM. Note that heating effects are not included in this calculation.

The PD I_{SC} is strongly dependent on the spectral distribution of emission of the LED. Along the same lines of the "matching factor" as introduced in [34], this dependence can be expressed by an emission-specific responsivity S defined as:

$$S = \int E(\lambda) \cdot \frac{I_{\mathrm{SC}}(\lambda)}{P_{\mathrm{opt}}} d\lambda, \tag{4}$$

Optics EXPRESS

where $E(\lambda)$ is the normalized spectral irradiance of the LED, such that $\int E(\lambda)d\lambda$=1. $I_{SC}(\lambda)$ is the PD I_{SC} when illuminated by a unidirectional monochromatic source having a fixed optical power P_{opt}. In Fig. 5(a) the TCAD simulated (in Sentaurus vL-2016.03) spectral repsonsivity of the PD, defined as $I_{SC}(\lambda)/P_{opt}$, is shown at T_0 = 300 K, excluding any heating effect. Default λ-dependent values of α_{Si} (= $4\pi k/\lambda$) at a fixed T_0 = 300 K were used. Figure 5(b) plots the integrand in the right hand side of Eq. (4) as a function of λ with $E(\lambda)$ being obtained from the measured EL spectra. The value of the emission specific responsivity S in AMLED operation is 100 times higher than in FMLED operation. This is expected due to a higher $\alpha_{Si}(\lambda, T_j)$ of the PD junction [35, 36] for shorter λ. The overall link efficiency η is discussed in the next two sections.

5. Coupling efficiency and waveguide in FM LED operation

In forward mode operation, the IQE of Si FMLEDs is reported to be $\sim 10^{-3}$ [4]. Figure 6 shows the measured coupling quantum efficiency η versus I_{FMLED} for different values of D at T_0 = 300 K. A gradual increase in η is observed with increasing I_{FMLED}. This trend indicates that the current is mainly diffusion-dominated [37], Auger recombination in the LED is not significant and the non-radiative recombination process is mainly Shockley-Read-Hall [35], the rate of which decreases with increasing I_{FMLED}.

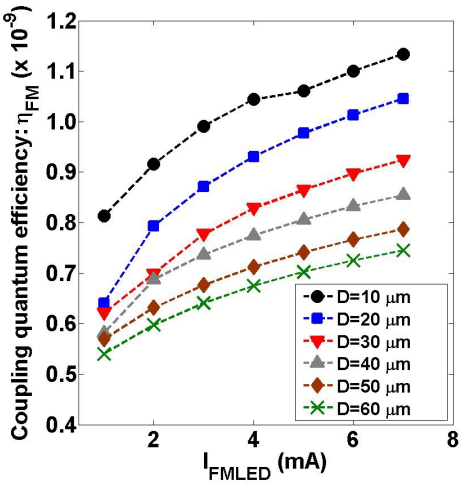

Fig. 6. Measured η_{FM} versus I_{FMLED} for different values of D at T_0=300 K.

Figure 7(a) shows the measured I_{SC} of the PD versus D for three values of I_{FMLED}. I_{SC} decreases monotonically with increasing D. The mean rate of attenuation γ_{FM} is low: $\approx$ 0.072 dB μm^{-1}. Pure isotropic transmission cannot explain this D-dependence because it would have resulted in a sharper attenuation ($\propto D^{-2}$), which is not observed. The trend can be explained by the formation of two lateral slab waveguides in our design as shown in Fig. 7(b). The back-end waveguide has a high index Si_3N_4 core sandwiched between a lower and an upper SiO_2 cladding layer formed by the STI and the inter-metal dielectric respectively. These dielectrics have a low absorption in the entire spectral range of interest [38, 39]. The high index SOI layer forms an additional waveguide with low absorption losses for photons with $\lambda > 1$ μm [33]. For simplicity, we assume that propagation occurs at near critical angles of incidence (θ_c). Hence, the effective index of the combined waveguide along the propagation direction (x-axis) is $n_{core} \cdot \sin\theta_c \approx n_{SiO2}$, where n_{core} represents the refractive index of the nitride or the SOI core layer. Consequently, the

Optics EXPRESS

observed D-dependence is captured in the propagation efficiency η_{prop} and is primarily due to the reduction in the lateral aperture of the PD as derived using geometrical ray optics as follows.

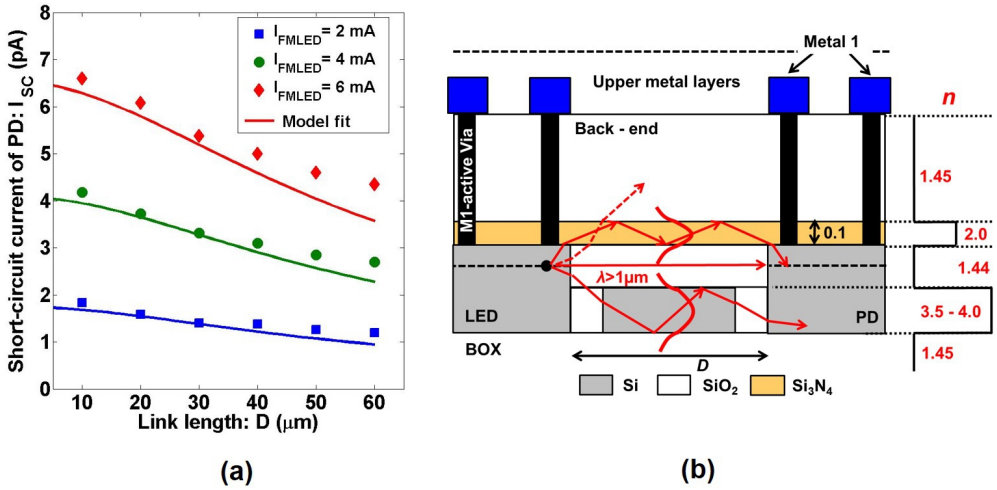

Fig. 7. (a) Measured and modeled I_{SC} of the PD versus D for three values of I_{FMLED}. I_{SC} decreases with increasing D as the angular aperture of the PD reduces. (b) Simplified cross-section of the link showing the position of two possible waveguides in FM coupling and the refractive indices for each material. An exemplary ray diagram and a fundamental mode wavefront are shown in each waveguide for a point source of light at the LED junction.

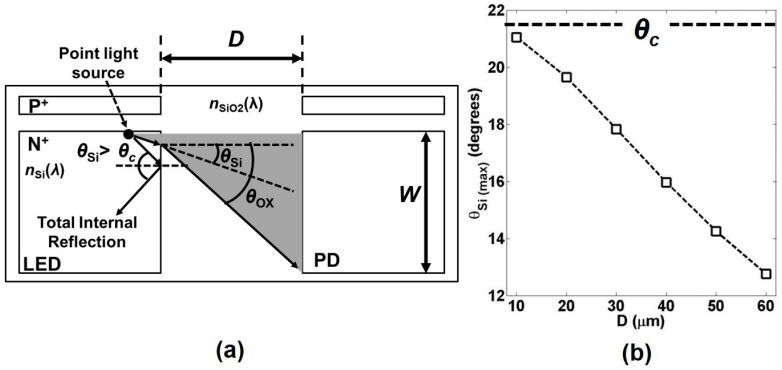

Fig. 8. (a) Simplified 2-D ray diagram of the top-view of our design, with $W \approx 45$ μm. Photons that are incident below the critical angle θ_c can emerge into SiO_2 prior to being guided through the nitride or the SOI layer. (b) Calculated maximum angular aperture of the PD for increasing D.

Figure 8(a) shows a simplified 2-D ray diagram of the top-view of our design for a point source of light. According to Snell's law, the effective 2-D aperture $\theta_{Si(max)}$ of the PD can be defined as the largest angle of incidence at the Si-SiO_2 interface for which the emergent ray is intercepted by the PD active area:

Optics EXPRESS

$$\theta_{\mathrm{Si(max)}}(D,W) = \sin^{-1}\left[\frac{n_{\mathrm{SiO2}}}{n_{\mathrm{Si}}\cdot\sqrt{1+\left(\frac{D}{W}\right)^2}}\right], \tag{5}$$

where n_{SiO2} and n_{Si} are the average refractive indices over the spectral range of SiO_2 and Si respectively. Note that $\theta_{\mathrm{Si(max)}}$ has an upper bound of $\theta_c \approx 21^o$, which is the critical angle at the Si-SiO_2 interface. As D increases for a fixed W (as in our experiment), $\theta_{\mathrm{Si(max)}}$ decreases (as shown in Fig. 8(b)), leading to a proportional reduction in the optical coupling. In addition, the absorption losses in the core and cladding are also D-dependent [40]. We can model these combined effects using the following relation:

$$I_{\mathrm{SC}}(D) = a\cdot\theta_{\mathrm{Si(max)}}\cdot\exp\left(-b\cdot D\right), \tag{6}$$

where a and b are fit parameters obtained using the least squares method. A good agreement is obtained between the modeled and measured trends as shown in Fig. 7(a). The fit value of a is proportional to $I_{\mathrm{SC}}(D = 10\ \mu\mathrm{m})$. The fit value of $b \approx 10\ \mathrm{cm}^{-1}$ is in good agreement with the reported [33] $\alpha_{\mathrm{Si}}(\lambda = 1.1\ \mu\mathrm{m})$. This indicates that the SOI waveguide is dominant in FM coupling.

6. Coupling efficiency and waveguide in AM LED operation

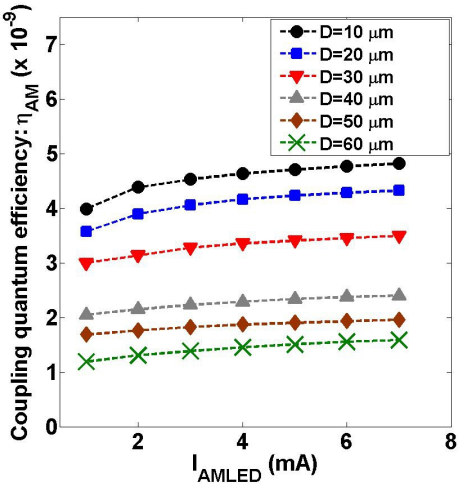

Fig. 9. Measured η_{AM} versus I_{AMLED} for different values of D at $T_0 = 300$ K. A heat sink is present in these designs.

The avalanche mode EL spectrum of the LED peaks in the visible range as shown in Fig. 3(a). The IQE of Si AMLEDs is reported to be $\sim 10^{-5}$ [12]. Figure 9 shows the measured η versus I_{AMLED} for different values of D. Note that a heat sink is present in these designs. The dependency of η on I_{AMLED} reflects the efficiency of radiative recombination in the AMLED, which is sensitive to the current level. We observe a weakly increasing η with increasing I_{AMLED}, indicating that the injection level is moderate enough not to cause a droop in the radiative efficiency owing to Auger recombination [35]. Further, η is observed to be relatively less sensitive to I_{AMLED} as compared to the situation in forward mode. This is because I_{AMLED} is dominated by impact ionization, which has a stronger bias dependence [41] as compared to that of forward mode diffusion current.

Optics EXPRESS

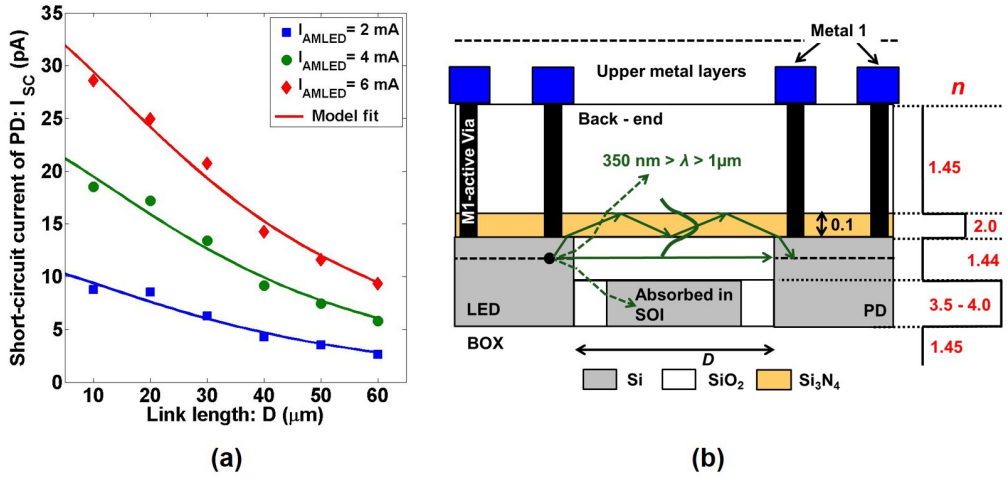

Fig. 10. (a) Measured and modeled I_{SC} of the PD versus D for three values of I_{AMLED}. I_{SC} decreases with increasing D as the angular aperture of the PD reduces. (b) Simplified cross-section of the link showing the position of the back-end waveguide in AM coupling.

Comparing Fig. 9 with Fig. 6, we also observe that for a given D and LED current, the coupling quantum efficiency in AM is always higher than in FM. This is mostly due to the combined effect of a lower AMLED IQE and a stronger AMLED-PD spectral overlap as compared to that of the FMLED (see Fig. 5(b)).

Figure 10(a) shows the measured and modeled I_{SC} of the PD versus D for three values of I_{AMLED}. I_{SC} decreases monotonically with increasing D. The mean rate of attenuation $\gamma_{AM} \approx 0.195$ dB μm^{-1}. Due to the small absorption lengths (~ 1 μm) in Si for short wavelengths emitted by the AMLED, the SOI layer does not serve as a WG. Thus, only the back-end WG formed by the high index Si_3N_4 core and the surrounding SiO_2 cladding can serve as the waveguide as shown in Fig. 10(b). The observed attenuation in AM coupling can also be modeled by Eq. (6). Fit parameter $a \propto I_{AMLED}$, and $b \approx 130$ cm^{-1}. Note that $\gamma_{AM} > \gamma_{FM}$, because AM coupling occurs only through the back-end dielectric WG. The optical thickness ($n_{core} \cdot t$) of the nitride core is ~ 10 times smaller than that of the SOI waveguide core, and the Si_3N_4 surface roughness is likely higher than that of the SOI. Both will lead to higher waveguide attenuation.

7. Heating in the AMLED and thermal coupling

DC operation: Heating is significant in AMLED operation and the photodiode junction temperature T_j is affected by the LED power consumption P_{AMLED} according to $\Delta T_j \propto P_{AMLED}$ [42,43]. Therefore, the rise in I_{SC} is partly contributed by this T_j (see section 4). Heating is more pronounced in SOI technology as compared to bulk Si technology due to the relatively poor thermal conductivity [44,45] of the buried oxide layer in the former.

Extracting ΔT_j and separating the independent contributions of EL intensity L and junction temperature T_j to the total I_{SC} are not possible analytically as V_{OC} and I_{SC} are related by an implicit equation (Eq. (3)) with coupled dependencies on L and T_j. We, therefore do it empirically [27] from the measured PD I-V characteristics by obtaining explicit and independent calibration maps: $I_{SC}(L)$, $I_{SC}(T)$, $V_{OC}(L)$, and $V_{OC}(T)$. Here T represents the temperature variable in general without distinguishing between the junction and the ambient. The relations of V_{OC} and I_{SC} of the PD with L and T are calibrated independently by using a commercial off-chip LED (to isolate optical from thermal effects) and by varying T_0 at a fixed L. The off-chip LED

Optics EXPRESS

emits at 650 nm with a FWHM of 40 nm, which approximately emulates the emission spectrum of the AMLED.

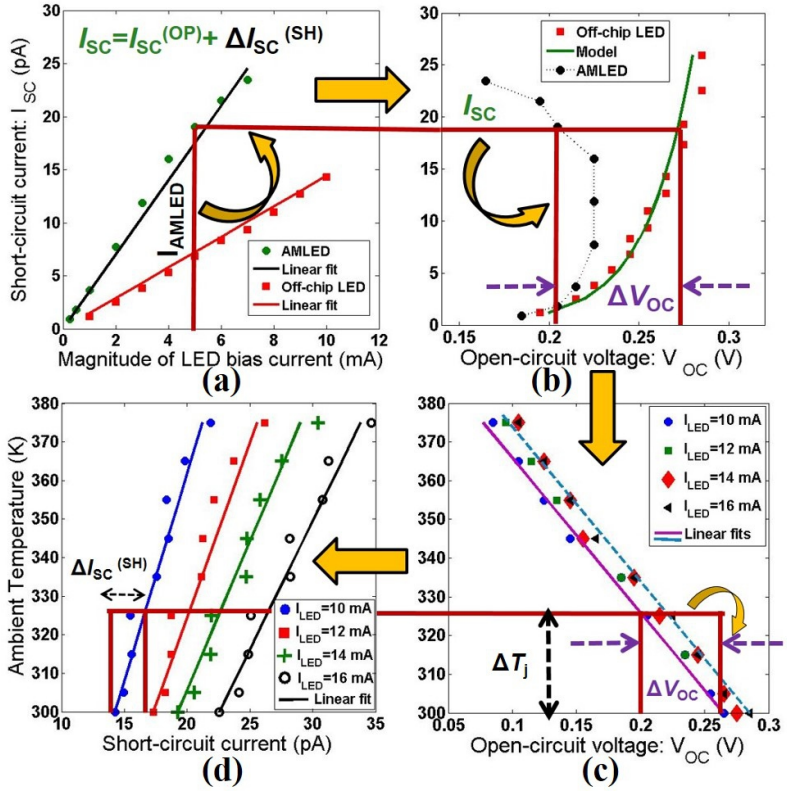

Fig. 11. De-embedding procedure for separating the contributions of L and ΔT_j to the total I_{SC} in AMLED operation in the default design (without heat sink): (a) I_{SC} versus I_{AMLED} at T_0 = 300 K. (b) Measured V_{OC} (black) for AMLED operation and the calibrated value (green) using the off-chip LED at T_0 = 300 K and modeled by Eq. (3). (c) Calibrated V_{OC}-T curve and (d) I_{SC}-T curve of the PD for various off-chip LED currents (and hence L).

The following steps are followed (as shown in Fig. 11) for extracting thermal coupling in DC operation in our default design (without heat sink).

Step 1: I_{SC} for a given I_{AMLED} is measured and is assumed to be the sum of $I_{SC}^{(OP)}$ and $\Delta I_{SC}^{(SH)}$, which represent the independent contributions of L (optical) and T_j respectively.

Step 2: Figure 11(b) shows the variation of I_{SC} versus V_{OC} of the PD during AMLED operation and the calibrated pure optical variation at T_0= 300 K obtained using the off-chip LED. The deviation of V_{OC} from the calibrated value, at the given I_{SC} obtained in step 1, is recorded.

Step 3: Figure 11(c) shows the calibrated $V_{OC}(T)$ for the PD for four different values of L of the off-chip LED. The slope of a linear fit of the (V_{OC},T) data points yield a mean temperature coefficient TC_{VOC} of -2.5 mV K^{-1}. The deviation ΔV_{OC} obtained in step 2, is then mapped onto the calibrated curve to obtain: $\Delta T_j = \frac{\Delta V_{OC}}{TC_{VOC}}$.

Optics EXPRESS

Step 4: Figure 11(d) shows the calibrated $I_{SC}(T)$ for the PD, with a mean temperature coefficient TC_{ISC} of 0.12 pA K^{-1}. The ΔT_j obtained in step 3 is then used to obtain $\Delta I_{SC}^{(SH)} = \Delta T_j \cdot TC_{ISC}$.

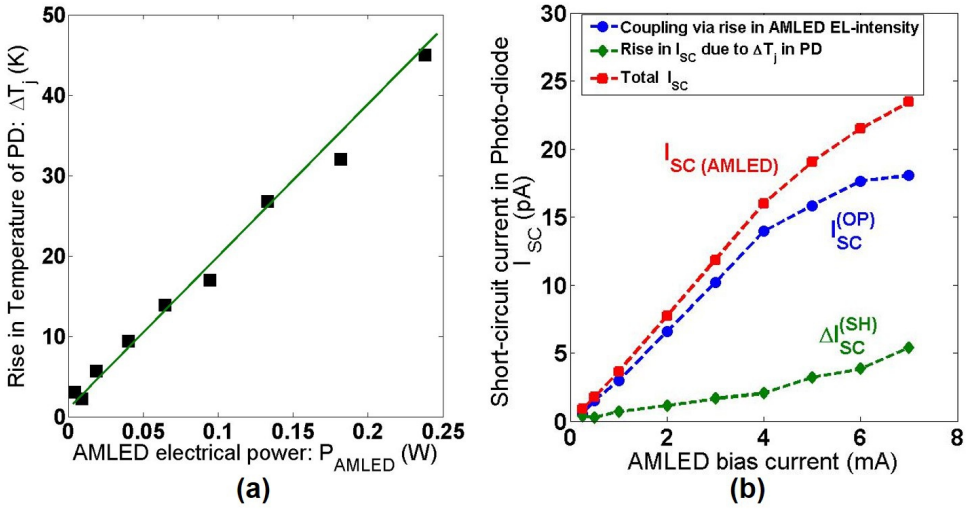

Fig. 12. (a) Rise in PD junction temperature (symbols) owing to heating in the AMLED in the default design of our optical link, following the procedure of Fig. 11. ΔT_j increases linearly with the LED electrical power P_{AMLED}. (b) The separated contributions of increasing L (blue) and increasing T_j (green) to the total measured I_{SC} (red).

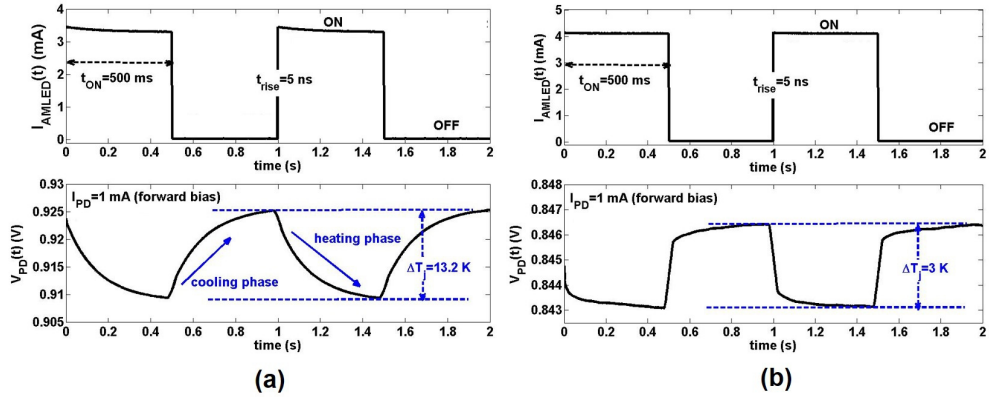

Fig. 13. Measured transient waveforms of the pulsed AMLED current $I_{AMLED}(t)$ (top) and the resulting $V_{PD}(t)$ (bottom) when the PD is forward biased with a constant current of I_{PD} = 1 mA (a) without heat sink and (b) with heat sink. V_{PD} shows a thermal RC relaxation behavior with a time constant τ_{TH} of 126 ms without heat sink and 40 ms with heat sink. Note that in this particular measurement, the LED is always operated in AM, which is the source of heat, and the PD is forward biased to suppress the optical dependence of $V_{PD}(t)$.

Optics EXPRESS

Figure 12(a) shows the extracted ΔT_j values at different P_{AMLED}. Figure 12(b) shows the separated components of I_{SC}. In the default design, around 13 % of the total I_{SC} is contributed by thermal coupling. The slope of $I_{SC}^{(OP)}$ - I_{AMLED} curve shows a gradual reduction for high values of I_{AMLED}. This is likely due to the combined T-dependencies of the IQE of AMLED and that of η_{WG}.

Transient operation: The (de-embedded) thermal coupling affects the bandwidth of the link, which in turn, affects the digital bit rates in data transfer. The bandwidth can be characterized by a thermal time constant $\tau_{TH} = R_{TH} \cdot C_{TH}$, where R_{TH} and C_{TH} are the effective thermal resistance and capacitance [42, 43] of the AMLED-link-PD system.

In order to extract τ_{TH}, the AMLED is pulsed between "on" (V_{AMLED}=25 V) and "off" (V_{AMLED}=15 V) states at a pulse repetition frequency (PRF) of 1 Hz with a 50 % duty cycle and a 5 ns rise time, as shown in Fig. 13(a). In this measurement, the PD is biased at a constant forward bias current I_{PD} = 1 mA. This bias ensures that V_{PD} is sensitive only to T_j with a measured temperature coefficient $\partial V_{PD}/\partial T_j$ of -1.2 mV K^{-1}, and that $\partial V_{PD}/\partial L$ at a constant T_j and constant I_{PD} is negligible.

During the "on" phase, the AMLED heats up leading to the heating of the PD, which reduces $V_{PD}(t)$. In the "off" (cooling) phase, $V_{PD}(t)$ relaxes back to its ambient value, exhibiting in both phases a first-order thermal RC behavior with τ_{TH} = 126 ms. Note that the electrical time constant of our set-up (~ 5 ns) contributed by the PD and wiring parasitics is negligible compared to τ_{TH} and hence does not affect our measurement.

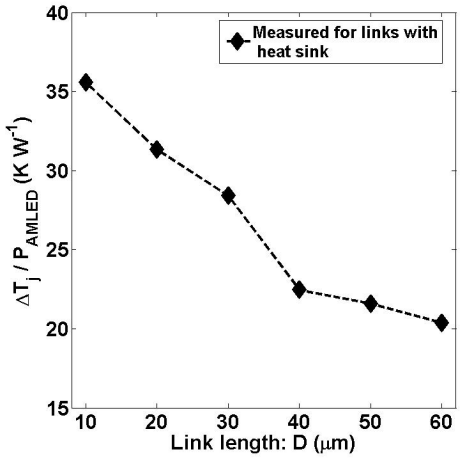

Fig. 14. Measured ΔT_j of the PD per unit P_{AMLED} versus increasing D showing a monotonic decreasing behavior. A heat sink is present in the links used in this measurement.

Effect of heat sink: ΔT_j can be reduced by including heat sinks. The heat sink we realized, significantly reduces the effective R_{TH} of the link and thereby leads to a 6 times reduction in ΔT_j in DC operation (~ 30 K W^{-1}) compared to the same link without the heat sink (~ 180 K W^{-1}). The reduction of R_{TH} also reduces τ_{TH} to 40 ms as shown in Fig. 13(b).

Effect of link length: The link length D directly impacts the thermal propagation. Using pulsed measurements in all these designs at a PRF of 1 Hz, similar to the one in Fig. 13(b), a monotonic decrease in ΔT_j per unit P_{AMLED} with increasing D has been obtained as shown in Fig. 14. Thus longer links have less thermal crosstalk, in agreement with a thermal lumped π-network model

Optics EXPRESS

with effective lateral (D-dependent) and vertical components of R_{TH}.

8. Discussion and design recommendations

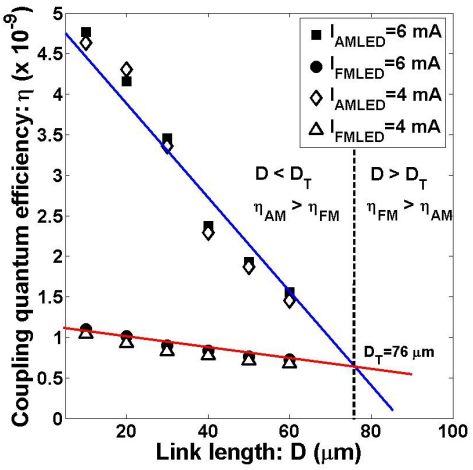

Fig. 15. Measured coupling quantum efficiency η in AM and FM coupling versus link length D for our designs. A linear extrapolation of the data yields a cross-over point $D = D_T$ =76 μm.

The main findings reported in sections 5 to 7, and their implications are as follows:

1. Within our measured range of I_{LED}, $\eta_{AM} > \eta_{FM}$. This result is an interplay of competing phenomena, encompassing η_{LED}, η_{WG} and η_{PD}. Nonetheless, we show that both FM and AM coupling in standard CMOS is feasible.

2. The coupling efficiency η decreases monotonically with increasing D. The rates of attenuation γ_{FM} and γ_{AM} are observed to be almost independent of the LED current. Further, $\gamma_{FM} < \gamma_{AM}$.

3. The different rates of attenuation in FM and AM coupling leads, for our design, to a cross-over point in coupling efficiency around $D = D_T \approx 76$ μm, where the extrapolated measured values intersect as shown in Fig. 15. This indicates that for $D < D_T$, avalanche mode operation yields a higher η, while for longer link lengths forward mode operation of the LED is preferred from a coupling efficiency point-of-view.

4. Measured PD I_{SC} is in the order of 10 pA in DC operation at T_0 = 300 K. For our optical link, this would enable data communication with an output (PD) referred signal-to-noise ratio (SNR) of ~ 15 dB for a bandwidth B of, for e.g., 1 MHz, where SNR = $10 \cdot \log\left[\frac{I_{SC}^2}{2 \cdot q \cdot I_{SC} \cdot B}\right]$. Here shot noise is the main contributor for noise power. Owing to such a low SNR, SPAD based receivers are needed to achieve high-speed data transfer through our link.

5. Heating in the AM operation of the LED leads to an increase in the PD junction temperature T_j. During on-off keying of the AMLED, this leads to a parameter shift in the PD. However, given the significantly long thermal time constants (in the range 40-120 ms), no thermal

Optics EXPRESS

data communication is expected during high speed opto-coupling; thermal coupling will at most lead to DC offsets at the receiver end.

6. AM coupling consumes ~ 10 times higher electrical power (in the LED) than FM coupling. However, the reported Si AMLED switching speed (~ GHz) is ~ 10^3 times higher than that reported for Si FMLEDs (~ MHz). Combined, this indicates that, for digital data communication, a ~ 100 times reduction in "energy per bit" can be achieved in AM coupling as compared to FM coupling in Si.

From the analysis in this paper we can formulate several design recommendations to improve the optical link, and in particular its coupling quantum efficiency.

Coupling in forward mode: To enhance η_{LED}, the spacing between the contact and n^+ diffusion edge can be increased, which reduces the diffusion current [37]. T_{Fresnel} can be increased by having only one MTI (instead of two) for galvanic isolation between the LED and the PD. η_{PD} can be enhanced by having both d_{PD} and W to be $> \alpha_{\mathrm{Si}}^{-1}(\lambda)$, where $\alpha_{\mathrm{Si}}^{-1}(\lambda)$ is the absorption length in Si. η_{prop} can be increased by removing the STI and the nitride layer. The resulting single SOI WG will have a greater optical thickness ($n_{\mathrm{Si}} \cdot t_{\mathrm{SOI}}$) and lower absorptive losses.

Coupling in avalanche mode: η_{LED} can be enhanced by increasing the perimeter to area ratio. The LED dimension in the direction of optical propagation can be reduced to the order of $\alpha_{\mathrm{Si}}^{-1}(\lambda)$. In addition, reducing the magnitude of V_{BR} of the AMLED can not only increase its power efficiency [13] but also reduces the parasitic thermal coupling. η_{PD} can be enhanced by having a lower doping level, which increases the depletion width and hence the responsivity. For links with SPAD based detectors, this recommendation is beneficial from the viewpoint of having a low dark count rate and high photon detection probability [25]. For the waveguide, η_{in} (or η_{out}) can be enhanced by increasing the contact area between the EL-region of the LED (or the PD active area) and the nitride core. Lastly, η_{prop} can be enhanced by patterning the WG on the x-y plane, which would reduce the effect of D-dependent angular aperture of the PD.

Improving the coupling quantum efficiency η is beneficial for increasing the achievable bandwidth of the optical link, when used for intra-chip data communication. It should be noted that although avalanche-mode LEDs in Si have been shown to exhibit GHz range small-signal modulation speeds [14], the maximum data rate is limited by the SNR at the output of the optical receiver. A 3 Gb/s optical receiver with off-chip illumination (λ = 850 nm) was reported [46] using PDs in standard 180 nm CMOS, where the input optical power determines the SNR and thereby the bit error rate. On the other hand, if optical intensities are low (like in our monolithic link), high-speed communication is feasible by using highly sensitive SPAD based receivers, which are sensitive to the number of photons received per bit, and thereby relies on η. Prior art reported SPADs [25, 26] in the same SOI technology. Here, the maximum data rate is limited by the dead-time of the SPAD (depends in turn on bit error rate specifications). For example, a dead-time of ~ 100 ns was demonstrated in the work of [26] that translates into a maximum data rate in the order of ~ 10 Mb/s. Measuring the maximum achievable data rate in our optical link requires high-speed measurements with RF de-embedding test structures, which we do not have at this time, and is thus still open to future research.

9. Conclusions

1. A monolithic, galvanically isolated, laterally-coupled and wide-spectrum (350 nm $<\lambda<$ 1270 nm) optical link in 0.14 μm silicon-on-insulator CMOS technology has been demonstrated. Optical coupling has been analyzed in both forward and avalanche mode LED operation, quantified by the short-circuit current in the photodiode.

Optics EXPRESS

2. The link exhibits a higher coupling quantum efficiency in avalanche mode LED operation as compared to forward mode LED operation. Coupling, especially through shorter wavelengths in avalanche mode, is made feasible via silicon dioxide and other inter-metal dielectrics like silicon nitride that form low-attenuation waveguide for the photons.

3. High power dissipation and heating in the avalanche mode LED leads to an increase in the junction temperature of the photodiode, observed to be 180 K W^{-1} (without heat sink) in DC operation of the LED. This is reduced to 30 K W^{-1} by integrating a heat sink. Measured thermal time constants of our design are 120 ms (without a heat sink) and 40 ms (with a heat sink).

4. Further, the coupling quantum efficiency has been experimentally shown to be monotonically decreasing with increasing link length, in agreement with a model that combines geometrical optics and attenuation.

The presented optical link is a potential solution for integrated wide-spectrum optical interconnects for smart power applications (e.g. level shifters) and intra-chip data communication in standard CMOS, when integrated with highly sensitive detectors (e.g. single photon avalanche-diodes) that compensate for the low photon-emission fluxes.

Funding

Dutch Technology Foundation (STW) (HTSM 2012, Project 12835).

Acknowledgments

The authors would like to thank NXP Semiconductors B.V. for fabricating the devices, S.M. Smits and J.P. Korterik (MESA+ Institute for Nanotechnology, University of Twente) for the experimental support and P.G. Steeneken and M. Swanenberg from NXP Semiconductors for their valuable discussions and chip finishing. The authors also are thankful to the reviewers for their constructive comments which have benefitted this paper.